

## Charge transfer in cold $\text{Yb}^+ + \text{Rb}$ collisions

Elvira R. Sayfutyarova,<sup>1,\*</sup> Alexei A. Buchachenko,<sup>1,2,†</sup> Svetlana A. Yakovleva,<sup>3</sup> and Andrey K. Belyaev<sup>3,‡</sup>

<sup>1</sup>*Department of Chemistry, M.V. Lomonosov Moscow State University, Moscow 119991, Russia*

<sup>2</sup>*Institute of Problems of Chemical Physics RAS, Chernogolovka, Moscow District 142432, Russia*

<sup>3</sup>*Department of Theoretical Physics and Center for Advanced Study, Herzen University, St. Petersburg 191186, Russia*

(Received 17 March 2013; revised manuscript received 15 May 2013; published 29 May 2013)

Charge-transfer cold  $\text{Yb}^+ + \text{Rb}$  collision dynamics is investigated theoretically using high-level *ab initio* potential energy curves, dipole moment functions, and nonadiabatic coupling matrix elements. Within the scalar-relativistic approximation, the radiative transitions from the entrance  $A\ ^1\Sigma^+$  to the ground  $X\ ^1\Sigma^+$  state are found to be the only efficient charge-transfer pathway. The spin-orbit coupling does not open other efficient pathways, but alters the potential energy curves and the transition dipole moment for the  $A$ - $X$  pair of states. The radiative, as well as the nonradiative, charge-transfer cross sections calculated within the  $10^{-3}$ – $10\ \text{cm}^{-1}$  collision energy range exhibit all features of the Langevin ion-atom collision regime, including a rich structure associated with centrifugal barrier tunneling (orbiting) resonances. Theoretical rate coefficients for two Yb isotopes agree well with those measured by immersing  $\text{Yb}^+$  ions in an ultracold Rb ensemble in a hybrid trap. Possible origins of discrepancy in the product distributions and relations to previously studied similar processes are discussed.

DOI: [10.1103/PhysRevA.87.052717](https://doi.org/10.1103/PhysRevA.87.052717)

PACS number(s): 34.20.Cf, 34.70.+e, 34.50.Cx

### I. INTRODUCTION

Ongoing efforts in the creation of cold atomic and ionic ensembles, as well as in their subtle manipulation, have been recently merged in preparation and study of the hybrid ion-atom systems [1–10]. This signifies the important step towards probing, understanding, and exploring ion-neutral interactions and collisions at sub-Kelvin temperatures. Elastic and momentum transfer collisions may serve as the means of cooling of both neutral [11–14] and charged [3,4,9] components. Ion-atom collisions resulting in charge transfer are of interest for a prototype of reactive processes and suggested to lead to gas-phase “metal-to-insulator” transitions at microkelvin temperatures [15].

Elastic, as well as resonant charge transfer, ion-atom collision dynamics is well understood theoretically [13,16]. A high-energy limit mediated by a short-range exchange interaction transforms to the so-called Langevin regime when a collision energy becomes comparable to a long-range induction interaction. When a collision energy decreases further, the quantum regime with its threshold laws for each partial wave is attained. This limit has been thoroughly considered within the multichannel quantum defect theory [17–20], but not yet reached experimentally.

Preparation of cold ion-atom systems is achieved in a hybrid trap by bringing in contact atomic and ionic ensembles or by creating ions via photoionization of cold atoms [2,4,5,7,13,14,21]. Collision- or photoinduced processes in Coulomb crystals can also be studied below 10 K [1,22,23] providing that the neutrals are cooled or decelerated [24]. However, in all cases the motion of ion(s) in the trapping field creates an unavoidable inherent source of a kinetic energy that imposes the limits on cooling [25]. Effective temperatures of

a few tens of millikelvins attained experimentally [2,5] still correspond to the Langevin regime with its complex dynamics sensitive to the global ion-atom potentials, transition moments, and coupling matrix elements. In addition, laser cooling creates an appreciable amount of electronically excited species, which further complicate the dynamics [7,26].

This explains the need for thorough theoretical studies that account for specific features of the particular perspective system. Resonant charge transfer has received more attention, with the focus on the model alkali or alkaline-earth (e.g., Refs. [16,27,28]) and  $\text{Yb}^+ + \text{Yb}$  [29] systems. For the nonresonant case, a few combinations of alkaline-earth-metal ions and alkali-metal atoms [13,14,30–33], as well as  $\text{Yb}^+$ ,  $\text{Ba}^+ + \text{Ca}$  collisions [6,26], were considered. Accurate *ab initio* calculations that back most of these studies revealed the complexity of charge-transfer pathways in the above systems. Strongly bound excited electronic states may well be involved in the dynamics by the nonadiabatic and/or spin-orbit couplings, or even directly upon laser cooling, preventing the use of simple two-state models [6,26,30,31,33]. Collision dynamics is complex itself being dominated by the resonances typical to the multiple partial-wave Langevin regime.

In the present paper we expand the theoretical experience considering the charge transfer in cold collisions between the ground-state  $\text{Yb}^+$  ion and Rb atom. Experimental studies by Köhl and co-workers [3,4], further extended to excited  $\text{Yb}^+$  ions [8], demonstrated the possibility of cooling an  $\text{Yb}^+$  ion in the ultracold Rb environment, gave the charge-transfer rate coefficient of the order of  $10^{-14}\ \text{cm}^3/\text{s}$  (the smallest one measured so far below 1 K) and characterized the product distributions. This system is attractive for further experimental studies since both  $\text{Yb}(^1S)$  and  $\text{Rb}(^2S)$  neutrals can be brought to degenerate gases [34–36] and combined with  $\text{Rb}^+(^1S)$  and  $\text{Yb}^+(^2S)$  ions for studying charge transfer from both “sides.” Rich isotope variety enables one to address the isotope and hyperfine structure effects. We performed accurate *ab initio* calculations of the potential energy curves, dipole moments, and nonadiabatic coupling matrix elements for the lowest electronic states of the  $(\text{YbRb})^+$  ion. We showed that within

\*Present address: Department of Chemistry, Frick Laboratory, Princeton University, NJ 08544.

†alexai@classic.chem.msu.ru

‡belyaev@herzen.spb.ru

the framework of the scalar-relativistic approximation the charge transfer can be considered by means of the two-channel model and that its radiative pathway is barely dominant. The vectorial spin-orbit interaction affects the electronic structure of the  $(\text{YbRb})^+$  ion, but does not produce a remarkable effect on the low-energy radiative charge transfer. Quantum scattering calculations within the range of collision energies relevant to the experiment show a rich resonance structure associated with orbiting resonances typical for the Langevin regime. Calculated rates agree well with the measured ones [4], although they reveal a less pronounced isotope effect. On the other hand, our study of single-collision dynamics results in some deviation in interpretation of the product distributions deduced experimentally.

## II. ELECTRONIC STRUCTURE

The electronic structure of the  $(\text{YbRb})^+$  ion was investigated *ab initio* using the MOLPRO program package [37]. All calculations were performed within the  $C_{2v}$  symmetry group with the origin of the electronic coordinates placed at the center of nuclear mass of the system composed of  $^{174}\text{Yb}$  and  $^{85}\text{Rb}$  isotopes and  $z$ -axis oriented along the internuclear vector  $\mathbf{R}$ .

### A. Techniques

Scalar-relativistic (SR) calculations were performed using the small-core 28-electron relativistic core potentials ECP28MDF with the supplementary contracted basis sets for both Yb [38] and Rb [39]. The sets of diffuse primitives of each of the *spdf* types with the exponents continuing two lowest exponents of the standard bases as an even-tempered sequence were added at each center to improve the description of induction and dispersion interactions. To evaluate the potential-energy curves (PECs) of the states that are the lowest ones in their symmetry (spatial and spin) representation, the restricted version of the coupled cluster method with singles, doubles, and noniterative triples, CCSD(T), was employed with the restricted Hartree-Fock reference. This type of calculation always included the set of  $3s3p2d2f1g$  bond functions (bf) [40] placed at the middle of the internuclear distance  $R$  and counterpoise correction for the basis set superposition error [41]. The  $\text{Yb}(4s^24p^64d^{10})$  shells were included in the core, whereas the rest of the electrons were correlated explicitly. The lowest excited singlet states were calculated by means of the equation-of-motion approach in coupled clusters with singles and doubles (EOM-CCSD) implemented in the same way. For excited triplets the multireference configuration interaction (MRCI) calculations with the Davidson correction [42] were performed with the reference wave functions built by the state-averaged complete active space multiconfigurational self-consistent field (CASSCF) method with active space spanned by the  $\text{Yb}(6s6p)$  and  $\text{Rb}(5s)$  atomic orbitals. The core set in the MRCI calculations consisted of  $\text{Yb}(4s^24p^64d^{10}5s^25p^6)$  and  $\text{Rb}(4s^2)$  atomic orbitals, whereas the  $4f^{14}$  shell of an Yb atom was correlated as fully occupied.

The similar MRCI method was used for spin-orbit (SO) calculations, but with the ECP28MWB effective core potential for Yb containing the SO part [43] and supplementary

segmented basis set [44] augmented by the *s2pdfg* diffuse functions [45]. The calculations were performed on the fine grid of the internuclear separation  $R$  from 1.9 to 40 Å.

### B. Scalar-relativistic results

The results of SR CCSD(T), EOM-CCSD, and MRCI calculations are shown in Fig. 1(a). At low collision energies it is sufficient to consider the states corresponding to the three lowest dissociation limits: (i)  $\text{Yb}(^1S) + \text{Rb}^+(^1S)$  that represents the final charge-transfer (CT) channel; (ii)  $\text{Yb}^+(^2S) + \text{Rb}(^2S)$ , the initial channel; and (iii) closed  $\text{Yb}^*(^3P^o) + \text{Rb}^+(^1S)$  CT channel that lies slightly above the entrance. Our best estimations for energies of excited limits  $16\,279\text{ cm}^{-1}$  (EOM-CCSD) and  $18\,646\text{ cm}^{-1}$  (MRCI) correspond well to the centers of the measured fine-structure multiplets,  $16\,750$  and  $18\,869\text{ cm}^{-1}$ , respectively [46]. It is evident that direct CT can only occur through  $A\ ^1\Sigma^+ - X\ ^1\Sigma^+$  interactions, either nonadiabatic or dipole.

To obtain the most accurate SR PECs for the relevant  $X\ ^1\Sigma^+$ ,  $a\ ^3\Sigma^+$ ,  $A\ ^1\Sigma^+$ ,  $b\ ^3\Pi$ , and  $2\ ^3\Sigma^+$  states, we took CCSD(T)-bf results for  $X$ ,  $a$ , and  $b$  as the reference. The  $A$ -state PEC was obtained by adding EOM-CCSD excitation energies to the ground PEC, whereas the MRCI results for  $\Pi - \Sigma$  splitting were used to obtain  $2\ ^3\Sigma^+$  PEC from the CCSD(T)-bf  $b\ ^3\Pi$  one. These *ad hoc* procedures aim to compensate the lower accuracy of EOM-CCSD and MRCI methods and incorporate the basis set superposition error correction. The resulting points were interpolated by cubic splines and joined smoothly to an analytical long-range (LR) function represented by the lowest-order  $-C_n/R^n$  asymptotic term. Finally, the PECs were shifted in energy to reproduce the true asymptotic limits. The parameters of so-obtained PECs are presented in Table I.

Accuracy of the *ab initio* PECs can be indirectly verified at long distances. LR behavior of the  $X$  and  $a$ ,  $A$  potentials is dominated by Yb and Rb induction, respectively. The finite-field CCSD(T) calculations estimated the static dipole polarizabilities of neutral atoms as  $\alpha_{\text{Yb}} = 142.2$  and  $\alpha_{\text{Rb}} = 318.2$  a.u., in perfect agreement with the recommended values  $\alpha_{\text{Yb}} = 139 \pm 7$  [47,48] and  $\alpha_{\text{Rb}} = 318.8 \pm 1.4$  a.u. [49,50]. The leading induction coefficients  $C_4 = \alpha_X/2$  are equal to 71 and 159 a.u., respectively, in reasonable correspondence with the fits to *ab initio* PECs (see Table I). Asymptotic dependence of the  $b\ ^3\Pi$  and  $2\ ^3\Sigma^+$  PECs originates from the charge-quadrupole  $\text{Rb}^+ + \text{Yb}^*(^3P^o)$  interaction. The results of Ref. [48] obtained within the more accurate *ab initio* approach allowed us to estimate the corresponding  $C_3$  coefficients as  $-7.2$  a.u. and  $14.4$  a.u., respectively. They agree with the fitted coefficients only qualitatively, but the LR behavior of the states correlating to the third dissociation limit is not crucial in the present context.

The permanent and transition dipole moments for the pair of  $^1\Sigma^+$  states were calculated by EOM-CCSD and MRCI methods, while the finite-field CCSD(T)-bf calculation was possible also for the ground  $X$  state. All the methods give similar results, although the MRCI  $A$ -state moment reveals the signatures of the mixing with higher lying states at the distances shorter than 4 Å. The  $A-X$  electronic transition dipole moment  $d_{AX}$  responsible for radiative CT is shown in Fig. 1(c).

TABLE I. Parameters of the lowest PECs of the  $(\text{YbRb})^+$  ion: Equilibrium distance,  $R_e$ ; state binding energy,  $D_e$ ; leading LR coefficient,  $C_n$ ; energy of the minimum with respect to the ground-state asymptotic limit,  $U_e$ ; and state dissociation asymptote,  $U_\infty$ , with respect to the ground asymptotic limit.

State	$R_e$ (Å)	$D_e$ ( $\text{cm}^{-1}$ )	$n; C_n$ (a.u.)	$U_e$ ( $\text{cm}^{-1}$ )	$U_\infty$ ( $\text{cm}^{-1}$ )
Scalar-relativistic PECs					
$X^1\Sigma^+$	4.28	3496	4; 72.9	-3496	0
$a^3\Sigma^+$	4.89	6176	4; 163.7	10574	16750
$A^1\Sigma^+$	7.31	836	4; 155.5	15914	16750
$b^3\Pi$	3.97	3218	3; -4.6	15650	18869
$2^3\Sigma^+{}^a$			3; 18.8		18869
SO-coupled PECs					
$X0^+$	4.28	3498	4; 72.9	-3498	0
$a0^-$	4.87	6312	4; 163.7	10438	16750
$a1$	4.88	6236	4; 163.7	10513	16750
$A0^{+b}$	7.30	837	4; 155.5	15912	16750
$A0^{+c}$	4.04	1849		14901	16750
$A0^{+d}$	5.78			16790	16750

<sup>a</sup>Repulsive PEC.

<sup>b</sup>Right minimum, corresponds to the  $A^1\Sigma^+$  SR state.

<sup>c</sup>Left minimum, corresponds to the  $b^3\Pi$  SR state.

<sup>d</sup>Avoided crossing maximum.

In addition to the transition dipole moment, two  $^1\Sigma^+$  states are coupled by the nonadiabatic coupling matrix elements (NACMEs) as defined in Sec. III. The first-order radial NACME was computed using the two-point finite-difference procedure [37] using the MRCI vectors built on the CASSCF wave functions obtained with averaging over the two lowest  $^1\Sigma^+$  states. It was checked that neither inclusion of the third state of the same symmetry into CASSCF averaging nor the use of the more accurate three-point differentiation procedure alter the results remarkably. The second-order radial NACME was approximated as the derivative of the first-order

one [51]. For two states of the same symmetry the first-order angular NACME, proportional to the orbital electronic angular momentum operators  $L_x$  and  $L_y$ , vanishes by parity. Nonvanishing is the second-order NACME represented by the  $L_x^2 + L_y^2$  operator. The one-electron part of the  $L_y^2$  operator ( $L_x^2$  is the same by symmetry) was calculated as the matrix element on the CASSCF wave functions. As shown in Fig. 2, the first-order radial coupling is expectedly much stronger than the second-order and angular ones. The mixing with the higher lying electronic states at short distances already noted for dipole moments affects NACMEs as well.

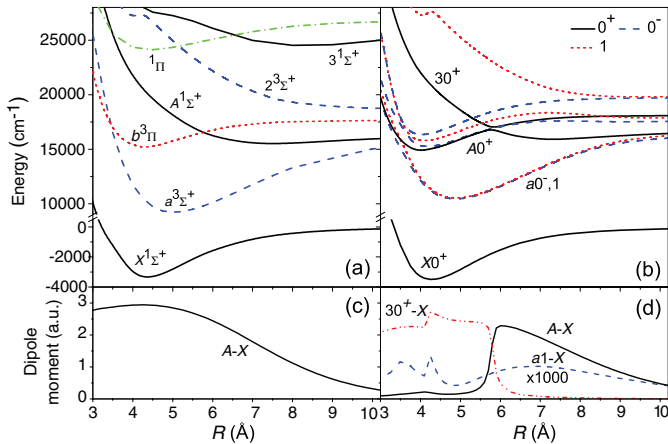


FIG. 1. (Color online) Potential energy curves and dipole moment functions for the lowest electronic states of the  $(\text{YbRb})^+$  ion. (a) Scalar-relativistic PECs. In addition to the states correlating to the three lowest asymptotic limits discussed in the text,  $3^1\Sigma^+$  and  $^1\Pi$  states correlating to the fourth  $\text{Yb}(^1P^o) + \text{Rb}(^1S)$  asymptote ( $26\,172\text{ cm}^{-1}$ , cf.  $25\,068\text{ cm}^{-1}$  [46]) are shown. (b) PECs for the lowest SO-coupled  $0^\pm$  and  $1$  states. (c) The scalar-relativistic  $A-X$  transition dipole moment. (d) The SO-coupled  $A-X$ ,  $a1-X$ , and  $30^+-X$  transition dipole moments.

### C. Spin-orbit coupling

The state-interacting MRCI SO calculations [52] were performed in the space spanned by the scalar-relativistic states

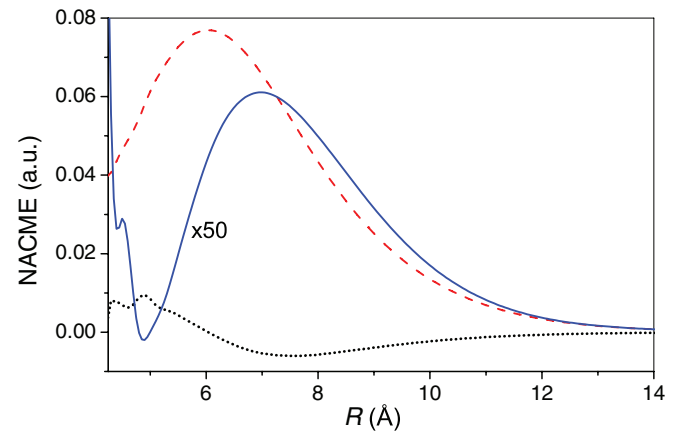


FIG. 2. (Color online) Nonadiabatic couplings between the  $X^1\Sigma^+$  and  $A^1\Sigma^+$  states: the first-order radial NACME (dashed line), the second-order radial one (dotted line), and the second-order angular NACME multiplied by 50 (solid line).

correlating to the three lowest dissociation limits. The SO matrix elements were evaluated for the Breit-Pauli operator using the inner part of the MRCI wave functions. The PECs described above were used as the diagonal SR part of the full Hamiltonian matrix. Relevant SO-coupled PECs are shown in Fig. 1(b) and characterized in Table I.

The states correlating to the lowest dissociation limits are weakly affected by the SO coupling. The only qualitative effect, the splitting of the  $a^3\Sigma^+$  state into the  $a0^-$  and  $a1$  components, is not significant. Much more pronounced is the interaction with the higher states correlating to an excited  $\text{Yb}^*$  atom. The asymptotic limit splits into three components that correspond to the  $^3P_j^o$ ,  $j = 0, 1$ , and  $2$ ,  $\text{Yb}^*$  fine-structure levels. The lowest  $^3P_0^o$  one gives the single  $0^-$  component that may interact with the  $a0^-$  state at short distances, whereas the second  $^3P_1^o$  gives  $0^+$  and  $1$  components. The former transforms the  $b^3\Pi-A^1\Sigma^+$  crossing into the avoided one giving the double-well  $A0^+$  PEC. The latter perturbs the repulsive wall of the  $a1$  potential. These changes also affect the transition dipole moments. The  $A$ - $X$  transition moment is similar to its scalar-relativistic precursor at distances larger than the avoided crossing point  $R \approx 6 \text{ \AA}$  and rapidly falls down at shorter distances [see Fig. 1(d)]. Instead, a significant dipole coupling occurs with the upper  $30^+$  state, which acquires charge-transfer character as the result of the crossing. The sum of the  $A$ - $X$  and  $30^+$ - $X$  transition moments is therefore similar to the scalar-relativistic  $A^1\Sigma^+-X^1\Sigma^+$  one. The SO interaction also allows the transition from the  $a1$  to the  $X$  state, but the corresponding dipole moment is negligible.

### III. NONRADIATIVE CHARGE TRANSFER

The nonradiative charge-transfer process in low-energy  $\text{Yb}^+ + \text{Rb}$  collisions can occur due to nonadiabatic transitions between the initial and the final molecular states induced by nuclear motion. We estimated its probability using the SR *ab initio* picture presented above [see Fig. 1(a)]. In this approximation, it is sufficient to consider only two states: the initial  $A$  and the final  $X$  ones, both of the  $^1\Sigma^+(\Lambda = 0)$  symmetry, whereas the spin restriction forbids the low-energy CT in the triplet manifold.

#### A. Theory

The nonadiabatic nuclear dynamics was studied within the formalism of the standard adiabatic (Born-Oppenheimer) approach described, for example, in Refs. [53–56]. The approach is based on a fundamental simplification, the Born-Oppenheimer separation of electronic and nuclear motions, leading to a fixed-nuclei electronic structure calculation and an appropriate treatment of nuclear motion based on the data calculated in the first step. This separation results in the total wave function expanded in terms of products of the electronic fixed-nuclei wave functions  $\Psi_j(\mathbf{r}, \mathbf{R})$ , the angular nuclear wave functions, and the radial nuclear wave functions,  $\mathbf{r}$  being a set of electronic coordinates. The electronic wave functions are calculated as described in the previous section. The angular nuclear wave functions are expressed via the generalized spherical harmonics [55,56]. The radial nuclear wave functions obey the system of coupled channel equations [55,56]. In

the present case of low-energy  $\text{Yb}^+ + \text{Rb}$  collisions, when nonadiabatic transitions occur only between two  $^1\Sigma^+$  states, the coupled channel equations for the radial nuclear wave functions  $\bar{F}_j^{J,E}(R)$  are reduced to the following equations (in a.u.):

$$\begin{aligned} & \left[ -\frac{1}{2\mu} \frac{d^2}{dR^2} + U_j(R) + \frac{J(J+1)}{2\mu R^2} - E \right] \bar{F}_j^{J,E} \\ &= \frac{1}{\mu} \sum_{k \neq j} \langle \Psi_j | \frac{\partial}{\partial R} | \Psi_k \rangle \frac{d\bar{F}_k^{J,E}}{dR} + \frac{1}{2\mu} \sum_k \langle \Psi_j | \frac{\partial^2}{\partial R^2} | \Psi_k \rangle \bar{F}_k^{J,E} \\ & \quad - \frac{1}{2\mu R^2} \sum_k \langle \Psi_j | L_x^2 + L_y^2 | \Psi_k \rangle \bar{F}_k^{J,E}. \end{aligned} \quad (1)$$

Here  $E$  is the collision energy measured from the asymptotic limit of the initial state  $A^1\Sigma^+$ ,  $J$  is the total angular momentum quantum number, which in case of the  $^1\Sigma^+$  states represents simultaneously orbital and rotational momenta of the nuclei,  $\mu$  is the reduced mass of the nuclei,  $j$  and  $k$  indices runs over  $A$  and  $X$ ,  $U_j$  is the adiabatic PEC, and the three terms in the right-hand side contain first- and second-order radial and angular NACMEs, respectively, defined as the integrals over the electronic coordinates  $\mathbf{r}$  and calculated as described in the previous section.

The coupled-channel equations (1) have their simplest and standard form due to the choice of coordinates: the Jacobi coordinates in which the vector  $\mathbf{R}$  connects the nuclei (for a fixed-nuclei treatment) and the set of electron coordinates  $\mathbf{r}$  is defined from the center of nuclear mass, the coordinates employed in the *ab initio* calculations described above. In these coordinates special care, e.g., by means of the reprojection method [56–58], should be taken in the asymptotic ( $R \rightarrow \infty$ ) region for calculating of nonadiabatic transition probabilities due to the fact that some radial NACMEs may have nonvanishing values, but in the present case all the treated NACMEs have zero asymptotes (see Fig. 2).

Due to the large energy splitting and small values of NACMEs, the nonadiabatic transition probabilities are expected to be small at low collision energies, and further simplification can be achieved by using the perturbation theory. The probabilities for a nonadiabatic transition  $A \rightarrow X$  due to the radial NACMEs (of both orders) can be approximated as [59]

$$\begin{aligned} P_{AX}^{\text{RAD}}(J, E) &= \frac{1}{4} \left| \int_0^\infty \langle \Psi_A | \frac{\partial}{\partial R} | \Psi_X \rangle \right. \\ & \quad \times \left[ F_A^{J,E} \frac{dF_X^{J,E}}{dR} - F_X^{J,E} \frac{dF_A^{J,E}}{dR} \right] dR \Big|^2, \end{aligned} \quad (2)$$

$F_{X(A)}^{J,E}(R)$  being an unperturbed scattering radial wave function (distorted wave) in the channel  $X(A)$  normalized by the probability current. For transitions induced by the angular NACME of the second order, the equations are similar to the coupled-channel equations in a diabatic representation, and the perturbation theory provides the following nonadiabatic transition probability:

$$P_{AX}^{\text{ANG}}(J, E) = \left| \int_0^\infty \frac{1}{R^2} [F_A^{J,E} \langle \Psi_A | L_x^2 + L_y^2 | \Psi_X \rangle F_X^{J,E}] dR \right|^2. \quad (3)$$



The nonradiative CT cross sections  $\sigma_{AX}^{\text{RAD}}$  and  $\sigma_{AX}^{\text{ANG}}$  due to the radial and the angular NACME are computed as a sum over the total angular momentum quantum number  $J$ :

$$\sigma_{AX}^{\text{RAD(ANG)}}(E) = \frac{\pi g_i}{2\mu E} \sum_J (2J+1) P_{AX}^{\text{RAD(ANG)}}(J, E), \quad (4)$$

$g_i$  being a statistical probability for population of the initial channel  $i$ . For the entrance  $A^1\Sigma^+$  channel,  $g_i = 1/4$ . Because of low collision energies treated the radial wave functions have to be calculated up to large internuclear distances, up to several thousands angstroms in the present case.

### B. Cross sections

The calculated  $A \rightarrow X$  nonradiative cross sections are presented in Fig. 3. All calculations were performed for the <sup>85</sup>Rb isotope. The <sup>174</sup>Yb isotope is assumed unless indicated explicitly. It is seen that the CT process induced by the angular NACME is roughly 14 orders of magnitude less efficient than that induced by the radial couplings. The reason is that the total electronic orbital momenta  $L$ , though not the good quantum numbers, are zero in the asymptotic  $R \rightarrow \infty$  limit. (In the united ion limit  $\text{Bh}^+$ , at least the  $X$  state should also have  $L = 0$  [60].) Nonvanishing angular NACMEs can only arise from the minor admixtures of excited states with different angular structure to the adiabatic electronic wave functions. In turn, the cross section due to the radial NACMEs is small on its own: The corresponding rate coefficient is roughly of the order of  $10^{-26}$  cm<sup>3</sup>/s at 1 K temperature. This is the consequence of both the large adiabatic splitting and weak interaction of the  $A^1\Sigma^+$  and  $X^1\Sigma^+$  states, resulting in small values of the radial NACMEs.

The nonradiative cross sections exhibit numerous resonances whose positions in the radial and angular counterparts

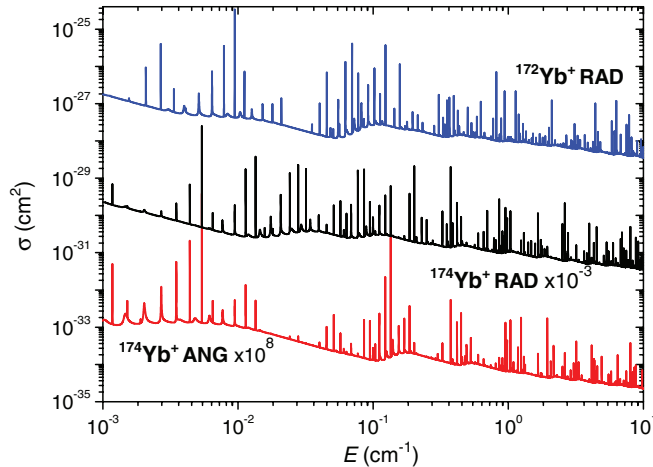


FIG. 3. (Color online) Nonradiative CT cross sections for Yb<sup>+</sup> + Rb collisions induced by NACMEs of different origins. The uppermost (blue) trace shows the cross section for <sup>172</sup>Yb<sup>+</sup> + Rb collisions due to the radial NACMEs. The second from the top (black) trace represents the same cross section for <sup>174</sup>Yb<sup>+</sup> + Rb collisions (multiplied by  $10^{-3}$ ). The bottom (red) trace depicts the cross section for <sup>174</sup>Yb<sup>+</sup> + Rb collisions due to the angular NACME (multiplied by  $10^8$ ).

are identical for the same Yb isotope. This structure, typical to the Langevin regime [13,16,28–30,33], arises from the tunneling through centrifugal barriers of the effective potential energy in combination with the polarization potential for the initial channel, as is shown in the next section. Isotope substitution alters the cross section insignificantly.

To conclude, the large mass of the system, vanishing electronic angular momenta of the  $X$  and  $A$  states, and their large energy separation in the interaction region suppress the nonadiabatic couplings and make the direct nonradiative CT process very inefficient. Inclusion of the SO couplings does not change the conclusion. For this reason, we did not exploit more thorough treatments of the nonadiabatic dynamics.

### IV. RADIATIVE CHARGE TRANSFER

The dipole coupling between the  $A$  and  $X$  states should provide a more plausible radiative CT mechanism. As far as the nonadiabatic effects are negligible, we estimated its efficiency using the standard adiabatic picture and commonly accepted quantum scattering approaches. Following the previous works on cold ion-atom collisions, we did not consider the effects of external fields and hyperfine structure.

#### A. Theory

Detailed description of the collision-induced spontaneous radiative transition from electronic state  $i$  to electronic state  $f$  is given by the frequency-resolved cross section  $d\sigma^{\text{R}}(E)/d\omega$ , where the collision energy  $E$  and the final energy  $E'$  define the emission frequency  $\hbar\omega = E - E'$ . Depending on the final PEC and the final energy, transitions may occur into the continuum [charge transfer in the strict sense; hereafter “charge exchange” (CE)] or bound [radiative association (RA)] levels. Within the Fermi golden rule (FGR) approximation the corresponding cross sections are expressed as [61–65]

$$\frac{d\sigma^{\text{CE}}(E)}{d\omega} = \frac{8\pi^2}{3} \frac{\mu^2}{k^3 k'} g_i \alpha^3 \omega^3 \sum_J (2J+1) \sum_{J'} H_{JJ'} D_{EJ,E'J'}^2 \quad (5)$$

and

$$\begin{aligned} \frac{d\sigma^{\text{RA}}(E)}{d\omega} &= \frac{8\pi^2}{3} \frac{\mu}{k^3} g_i \alpha^3 \sum_J (2J+1) \\ &\times \sum_{v'} \sum_{J'} \omega_{E,v'J'}^3 H_{JJ'} D_{EJ,v'J'}^2 \delta(\omega - \omega_{E,v'J'}). \end{aligned} \quad (6)$$

Here  $J$  and  $J'$  are the nuclear angular momenta in the initial and final states,  $v'$  is the vibrational quantum number of the final state with the energy  $E_{v'J'}$ ,  $\hbar\omega_{E,v'J'} = E - E_{v'J'}$ ,  $\alpha$  is the fine-structure constant,  $k^2 = 2\mu E$ ,  $k'^2 = 2\mu E'$ ,  $\delta(x)$  is the Dirac function, and  $H_{JJ'}$  is the standard Hönl-London factor.

The transition dipole moment matrix elements on the radial nuclear wave functions are defined as

$$\begin{aligned} D_{EJ,E'J'} &= \int_0^\infty F_i^{J,E}(R) d_{if}(R) F_f^{J',E'}(R) dR, \\ D_{EJ,v'J'} &= \int_0^\infty F_i^{J,E}(R) d_{if}(R) F_f^{J',v'}(R) dR. \end{aligned}$$

The choice of the coefficients in Eqs. (5) and (6) implies the normalization of distorted waves  $F_i^{J,E}, F_f^{J',E'}$  used in Ref. [64].

The total radiative cross section is given by

$$\begin{aligned}\sigma_{if}^R(E) &= \sigma_{if}^{\text{CE}}(E) + \sigma_{if}^{\text{RA}}(E) \\ &= \int_0^{\omega_{\text{max}}} d\omega \left[ \frac{d\sigma_{if}^{\text{CE}}(E)}{d\omega} + \frac{d\sigma_{if}^{\text{RA}}(E)}{d\omega} \right] \\ &= \int_0^{\omega_0} d\omega \frac{d\sigma_{if}^{\text{CE}}(E)}{d\omega} + \int_{\omega_0}^{\omega_{\text{max}}} d\omega \frac{d\sigma_{if}^{\text{RA}}(E)}{d\omega},\end{aligned}\quad (7)$$

where  $\omega_{\text{max}}$  is the maximum frequency that corresponds to a transition to the ground level  $v' = 0, J' = 0$ , whereas  $\omega_0$  frequency does to the ground-state dissociation limit. After substitution of Eq. (6) into Eq. (7), integration over  $\omega$  with  $\delta$  function transforms the last term of the latter into a sum over the discrete  $v', J'$  quantum numbers.

The closed expression for the total elastic cross section follows from the optical potential (OP) approach (see, e.g., Refs. [64,66–68], and references therein). Combined with the distorted wave approximation, it reads [64]

$$\sigma_{if}^R(E) = \frac{\pi}{k^2} g_i \sum_J (2J+1) \{1 - \exp[-4\eta_J(E)]\} \quad (8)$$

with

$$\eta_J(E) = \frac{2\pi}{3} \frac{\mu}{k} \alpha^3 \int_0^\infty F_i^{J,E} d_{if}^2(R) [U_i - U_f]^3 F_i^{J,E} dR. \quad (9)$$

For the  $A^1\Sigma^+ - X^1\Sigma^+$  or  $A0^+ - X0^+$  transitions under consideration,  $H_{JJ'} = J(2J+1)^{-1}$  if  $J' = J-1$ ,  $H_{JJ'} = (J+1)(2J+1)^{-1}$  if  $J' = J+1$ , and  $H_{JJ'} = 0$  otherwise.

## B. Cross sections

The radiative cross sections defined above were computed numerically using fine radial and energy grids and strict convergence criteria for partial wave summations. Accuracy of the OP cross sections was estimated as 3%, whereas the accuracy of the FGR calculations was within 5%–8% due to additional errors in integration over  $\omega$  and convergence of the wave functions very close to the dissociation limit of the ground state.

The total OP radiative cross section for the SR model (all the parameters,  $A^1\Sigma^+$ ,  $X^1\Sigma^+$  PECs and  $d_{AX}$  transition moment function, are taken from the SR calculations) for the collision energy range 0.001–10  $\text{cm}^{-1}$  are shown in Fig. 4(a) as the upper trace (multiplied by two). It gradually declines with collision energy increase in agreement with the Langevin capture cross section  $\sigma_L = 2\pi\sqrt{C_4/E}$  being five orders of magnitude smaller. The radiative CT cross section exceeds the nonradiative ones by 14 orders of magnitude and bears similar resonance structure. Analysis of the individual partial wave contributions allowed us to correlate the resonance energies with the positions of centrifugal barriers at certain  $J$ , as is shown in Fig. 5 for the low-energy cross section for collisions involving  $^{172}\text{Yb}$  and  $^{174}\text{Yb}$  isotopes. The cross-section structure consists of strong narrow resonances, which correspond to the tunneling deep under the centrifugal barriers, and weak broad resonances slightly below or above the

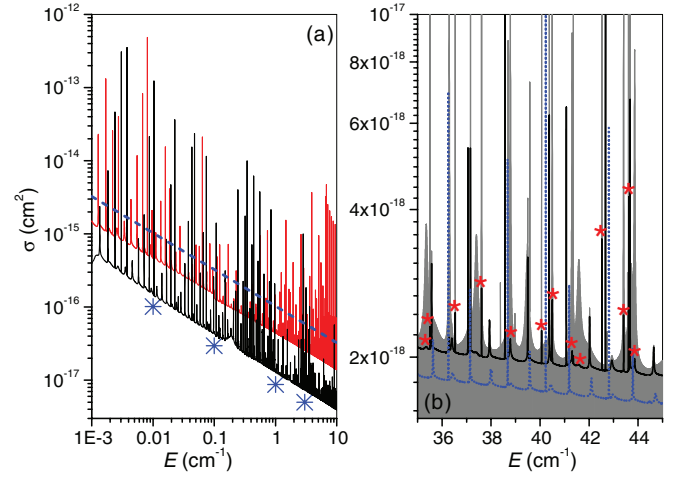


FIG. 4. (Color online) Total radiative  $A-X$  cross sections for the  $\text{Yb}^+ + \text{Rb}$  collisions calculated within the OP approximation. (a) Low-energy results for SR (upper trace, multiplied by two) and SO (lower trace) models. Asterisks represent the RA (free-bound) cross section from the FGR calculations for the SO model. Dashed line corresponds to the Langevin inelastic cross section multiplied by  $10^{-5}$ . (b) Cross sections near the potential barrier top of the  $A0^+$  state ( $40 \text{ cm}^{-1}$ ). Dotted and solid lines—SR and SO models, respectively. The shaded area presents the results of the “mixed” model calculations with the SO-coupled PECs and SR transition dipole moment. Asterisks indicate the resonance features of the SO cross section associated with the potential barrier.

barriers. All these findings signify the Langevin character of the  $\text{Yb}^+ + \text{Rb}$  cold inelastic collisions.

The total OP cross section computed within the SO model the SO-coupled  $X0^+$ ,  $A0^+$  PECs and the  $d_{AX}$  transition moment) are also presented in Fig. 4(a) (lower trace). Test calculations showed that the  $a1-X0^+$  radiative transition has a negligible probability. The SO model gives the cross section by 10% larger than the SR one with the same energy dependence, except the “bumps” at  $\sim 0.001$  and  $0.2 \text{ cm}^{-1}$ . Resonance structures of two traces are not identical, but the correlations are clearly visible at least below  $0.01 \text{ cm}^{-1}$  and were confirmed selectively by the partial wave analysis. However, the latter was of little help for seeking the effect of the potential barrier separating two wells of the SO-coupled  $A$ -state PEC [see Fig. 1(b)].

To elucidate it, we performed OP calculations with the “mixed” model that uses SO-coupled PECs but SR transition dipole moment. The results of three models are compared in Fig. 4(b) for collision energies close to the potential barrier top ( $40 \text{ cm}^{-1}$ ; see Table I). Preserving the Langevin-type structure similar to that of the SR cross section, the mixed cross section is dominated by additional very intense features significantly broadened at the background. They were attributed to the potential barrier tunneling or overbarrier resonances, since the penetration into the short-range well enhances the radiative transition probability (both Franck-Condon overlaps and transition moment value are more favorable here than in the long-range well; see Fig. 1). It is not the case for the consistent SO model, in which the transition moment decline suppresses the radiative transitions from the short-range well. Some features associated to the potential barrier, however, survive in the SO cross sections (the most visible are marked by asterisks

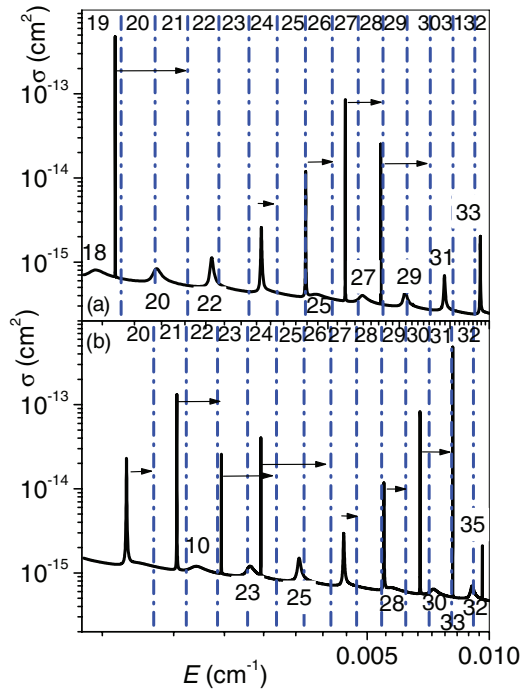


FIG. 5. (Color online) Low-energy resonance structure of the total radiative  $A$ - $X$  cross sections (the SR model, OP calculations). Vertical lines indicate the positions of centrifugal barrier top at  $J$  values given at the top of each plot. The resonances are assigned to  $J$  by arrows or  $J$  values given at the bottom of each plot. (a)  $^{172}\text{Yb}^+ + \text{Rb}$  collisions; (b)  $^{174}\text{Yb}^+ + \text{Rb}$  collisions.

in the figure). The same “mixed” model was used to confirm that the “bumps” mentioned above are also due to the potential barrier. As additional comments to Fig. 4(a), increase of the collision energy above the potential barrier does not lead to any drastic change of the cross section because the centrifugal term smoothes it for many partial waves, and increase of the SO cross section with respect to the SR one reflects the variation of the PECs rather than of the transition moment.

The results of the FGR calculations performed for the SO model at selected collision energies are presented in Table II. The total FGR cross section agrees with the OP one within the numerical accuracy justifying the optical potential approximation. Radiative association prevails over charge exchange: Within the energy range under study, transitions to the bound rovibrational levels of the  $(\text{YbRb})^+$  ion amount

TABLE II. Radiative cross sections (in  $10^{-17} \text{ cm}^2$ ) for charge transfer in the  $\text{Yb}^+ + \text{Rb}$  collisions calculated within the SO model at several collision energies  $E$ . Percentage contributions of RA and CE processes are given in parentheses.

$E$ ( $\text{cm}^{-1}$ )	FGR			OP total
	RA	CE	Total	
0.01	10.2 (71)	4.2 (29)	14.3	15.2
0.1	3.0 (69)	1.4 (31)	4.3	4.5
1	0.9 (69)	0.4 (31)	1.3	1.3
3	0.05 (67)	0.03 (33)	0.08	0.08

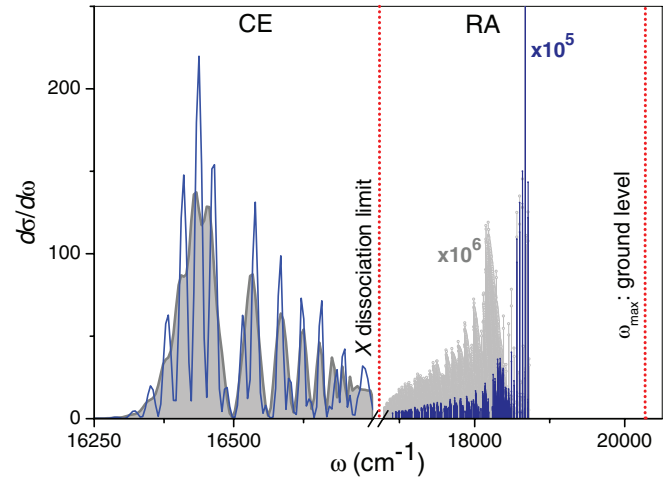


FIG. 6. (Color online) Frequency-resolved radiative cross sections normalized to the total cross sections, FGR calculations for the SO model. Lines correspond to the collision energy of  $0.01 \text{ cm}^{-1}$ ; shaded areas— $1 \text{ cm}^{-1}$ . Vertical dotted lines mark the borders of the free-bound spectrum set by the ground rovibrational level and dissociation limit of the  $X$  state. For RA, only the transitions with intensities exceeding 1% of the maximum one are shown.

to  $\sim 70\%$  of the total radiative charge transfer [see Fig. 4(a)]. Figure 6 compares  $A$ - $X$  spontaneous emission spectra at the collision energies  $0.01$  and  $1 \text{ cm}^{-1}$ . Increase of the collision energy leads mostly to “rotational” congestion of the spectrum due to involvement of higher partial waves. It is worth noting that all transitions are concentrated in the relatively narrow frequency range, from  $500 \text{ cm}^{-1}$  above the ground dissociation limit to  $2000 \text{ cm}^{-1}$  below ( $\sim 12\%$  of the available frequency range from  $0$  to  $20250 \text{ cm}^{-1}$ ).

## V. DISCUSSION

In this section, we first compare our theoretical results with experimental data available for  $\text{Yb}^+ + \text{Rb}$  collisions. Then we discuss them in a broader context of a few previous studies, mainly theoretical, on the cold CT processes in analogous nonresonant ion-atom systems.

### A. Implications to experimental data

In the experiments by Köhl and co-workers [3,4] the kinetic energy of a single  $\text{Yb}^+$  ion immersed in an ultracold Rb ensemble was varied by adding excess micromotion energy after displacement of an ion from the center of a trap. The binary-collision ion-loss rate coefficient determined in this way does not correspond to a conventional thermal rate constant for the Maxwell collision energy distribution at a certain temperature. For this reason, we also used the effective energy-dependent rate coefficient

$$R(E) = \sqrt{2E/\mu} \sigma_{AX}^R(E)$$

omitting negligible nonradiative CT contribution. This quantity derived from the OP calculations with the SO model is displayed in Fig. 7 within the energy range probed experimentally [4]. In agreement with the measurements and the trait of Langevin regime, the background rate coefficient

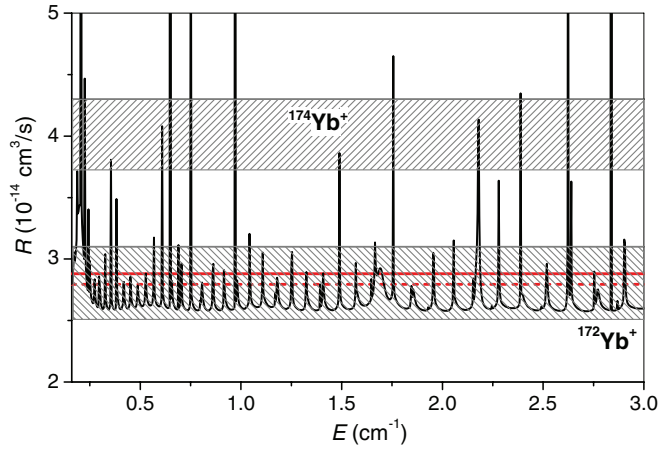


FIG. 7. (Color online) The energy-dependent CT rate coefficient  $R_{174}(E)$  (the SO model, OP calculations). Solid and dashed (red) lines represent the mean values for collisions with the  $^{174}\text{Yb}^+$  and  $^{172}\text{Yb}^+$  ions, respectively. Shaded areas represent the experimental error bars [4]. Rate coefficients are shown in the collision energy range studied experimentally.

does not depend on a collision energy. To define the average value, we took an arithmetic mean over a uniform grid of 10 000 points covering the relevant energy range from 0.15 to 3.25  $\text{cm}^{-1}$ . For the  $^{174}\text{Yb}$  ion, it amounts to  $2.9 \times 10^{-14} \text{ cm}^3/\text{s}$  in good agreement with the measured mean of  $(4.0 \pm 0.3) \times 10^{-14} \text{ cm}^3/\text{s}$  [4]. The background is  $\sim 2.6 \times 10^{-14} \text{ cm}^3/\text{s}$ , so the resonances contribute around 10% to the total rate. The SR model gives the mean rate of  $R = 2.4 \times 10^{-14} \text{ cm}^3/\text{s}$ .

Experiments with the  $^{172}\text{Yb}^+$  ions revealed a quite significant isotope effect,  $R_{174}/R_{172} \approx 1.4$  (see Fig. 7). Using the OP approximation (8) and assuming that the terms in the sum do not depend on the reduced mass, one arrives to small reverse scaling,  $R_{174}/R_{172} \propto (\mu_{172}/\mu_{174})^{3/2} \approx 0.994$ . It is supported by the fact that calculated background rate coefficients for two isotopes are hardly distinguishable. Nevertheless, the mean rate coefficients shown in Fig. 7 reproduce the reverse isotope effect. It originates from the resonant contribution and reflects slightly lower resonance density for the lighter isotope (careful inspection of Fig. 5 indeed reveals the less congested structure). Still, the theoretical rate coefficient ratio 1.03 is much smaller than the measured. More recent experiments for the same system have indicated dramatic effect of the hyperfine structure [8,69], which likely contributes to isotope effect as well.

Despite very reasonable agreement for the rate coefficient, our results do not reconcile to the measured product distributions. Experimentally, the probability of  $\text{Rb}^+$  ion production was found to be 35%, while the remaining 65% correspond to the loss of charged particle from the trap [4,8]. Our FGR calculations also give 30% for CE probability equivalent to  $\text{Rb}^+$  ion formation, but assign the remaining 70% to RA, formation of the stable  $(\text{YbRb})^+$  molecular ion not observed experimentally. Our calculations do not identify the trap loss channel, because, according to Fig. 6, all the CE products have the kinetic energy less than 500  $\text{cm}^{-1}$  at the trap depth of 1200  $\text{cm}^{-1}$  [4]. Several works [5–7,70] emphasized efficient secondary collision processes for  $\text{Ca}^+$ ,  $\text{Ba}^+$ , and

$\text{Rb}^+$  ions in contact with an ultracold Rb ensemble. This reason, however, was ruled out by Ratschbacher *et al.* [8], who failed to observe the  $(\text{YbRb})^+$  ion even at very short contact times. We assume that a more plausible explanation can be efficient photodissociation of the molecular ion to highly energetic products by cooling or trapping optical fields. More quantitative estimation may be useful for bridging the gap between theory and experiment.

## B. Other nonresonant cold ion-atom collisions

In many respects, neutral and singly ionized Yb is the  $4f$  analog of an alkaline-earth metal ( $M$ ). Indeed, a lot of similarity can be traced out in the interactions of the Rb atom with  $\text{Yb}^+$  and  $M^+$  ions. Due to mismatch in ionization potentials (IPs), the entrance  $M^+(^2S) + \text{Rb}(^2S)$  channel always lies above the ground  $M(^1S) + \text{Rb}(^1S)$  one, so the location and symmetry of excited  $M^* + \text{Rb}(^1S)$  CT channels determine the main qualitative difference. Binding of  $ns^2$  electrons decreases with  $n$  from Be to Ba as manifested in IP,  $ns^2 \rightarrow nsnp$  and  $ns^2 \rightarrow (n-1)dns$  promotion energies [46]. By these parameters, Yb most closely resembles Ca. However, in contrast to Yb, the excited  $\text{Ca}^*(^3P^o) + \text{Rb}$  CT channel is open and lying slightly below the entrance [7,30]. Moszynski and co-workers [31] studied theoretically the  $\text{Ba}^+ + \text{Rb}$  system, in which excited CT channels are energetically closed (see also Ref. [71]). However, these states correlate to  $\text{Ba}^*(^3D) + \text{Rb}(^1S)$  asymptote and exhibit a more complicated interaction with the entrance  $A^1\Sigma^+$  and  $a^3\Sigma^+$  states. In particular, the PEC of the  $A$  state has a double-well shape even in the nonrelativistic case. It should be expected that the  $\text{Sr}^+ + \text{Rb}$  system reveals more similarity to the  $\text{Yb}^+ + \text{Rb}$  one, but we are not aware of any work on it.

It appears that  $\text{Yb}^+ + \text{Rb}$  represents one of the simplest systems from the viewpoint of excited state effects. The use of lighter alkali-metal partners may further simplify the dynamics because increasing IP of the neutral will push the entrance channel down in energy. In the extreme case of Li, it lies only 7000  $\text{cm}^{-1}$  above the ground and almost 10 000  $\text{cm}^{-1}$  below the excited CT asymptote. Collisions with Li should be of special interest for cooling a trapped ion below the Langevin regime, as discussed by Cetina *et al.* [25].

Rellergert *et al.* [6] investigated cold  $\text{Yb}^+ + \text{Ca}$  collisions, in which only two states of the  $^2\Sigma^+$  symmetry separated asymptotically by 1140  $\text{cm}^{-1}$  are involved. Avoided crossing at long range presents an interesting feature of this system that facilitates the nonadiabatic CT pathway (see below). A similar picture should be expected for  $\text{Yb}^+ + \text{Sr}$ , whereas for  $\text{Yb}^+ + \text{Ba}$  the CT to excited  $\text{Ba}^+$  ion becomes possible. Among the nonresonant alkaline-earth-metal systems,  $\text{Ba}^+ + \text{Ca}$  has been studied by Sullivan *et al.* [26]. Here the CT process is endothermic and occurs from excited states of the ion.

It is also instructive to bring together scarce, mostly theoretical, data on the efficiency of distinct CT pathways. To do so on the same footing, we presented  $\epsilon_L$  coefficients—the ratios of the rate coefficient (cross section) to its Langevin inelastic value.

Our estimation for the nonradiative CT rate is vanishingly small,  $\epsilon_L \approx 10^{-17}$ . Much larger efficiencies,  $\epsilon_L \approx 5 \times 10^{-6}$  and  $10^{-3}$ , were reported for  $\text{Yb}^+ + \text{Ca}$  [6] and  $\text{Ca}^+ + \text{Rb}$  [30,33], respectively. In the former case, nonadiabatic



transitions should be dramatically enhanced by the above-mentioned avoided crossing. The latter coefficient in fact refers to the transition to the open excited CT channel, while the efficiency of the direct  $A$ - $X$  CT is of the order of  $10^{-6}$  [30]. The measured  $\epsilon_L \approx 10^{-3}$  for  $\text{Ca}^+ + \text{Rb}$  [10] confirms the nonradiative CT to excited channels. Indeed, the efficiency of the direct radiative CT was found to be by an order of magnitude lower,  $\epsilon_L \approx 7 \times 10^{-5}$  [10].

For radiative CT we got  $\epsilon_L \approx 1.5 \times 10^{-5}$ , in good correspondence with  $\text{Ca}^+ + \text{Rb}$  and  $\text{Ba}^+ + \text{Rb}$  collisions (theory  $\epsilon_L \approx 4 \times 10^{-5}$  [31] and  $5 \times 10^{-6}$  [71]; experiment  $10^{-4}$ – $10^{-3}$  [5] and  $< 2 \times 10^{-4}$  [71]). Calculations for  $\text{Yb}^+ + \text{Ca}$  provided  $\epsilon_L \approx 0.03$ , also in agreement with the measured rate [6]. The lowest radiative CT efficiency  $\epsilon_L \approx 10^{-7}$  was calculated for the  $\text{Ca}^+ + \text{Na}$  collisions [13,17].

Even less is known on the product distributions. The molecular ion was observed in the  $\text{Ca}^+ + \text{Rb}$  system together with  $\text{Rb}_2^+$  ion formed in the secondary collisions [7]. Studies of the  $\text{Ba}^+ + \text{Rb}$  [71] and  $\text{Yb}^+ + \text{Ca}$  [6] collisions revealed the same discrepancy between experiment and theory as we met here. In the former case, the  $(\text{BaRb})^+$  ion constitutes 30% of the ionic product, while the theory designates it as the barely dominant product of the radiative CT. An upper bound for  $(\text{YbCa})^+$  formation probability was estimated experimentally as 0.02%, whereas according to FGR calculations radiative association to molecular ion contributes 50%. It was speculated that the secondary RA processes may deplete the diatomic ion to heavier species such as  $(\text{Ca}_2\text{Yb})^+$  [6]. In our case the measurements failed to detect charged particles different from atomic ions and we proposed an alternative explanation—photodissociation of a molecular ion by a cooling and trapping optical field. Finally, calculations on  $\text{Ca}^+ + \text{Na}$  collisions showed even stronger predominance of the radiative molecular ion formation: RA to CE branching ratio was found to be around 20:1 [13,17].

The above overview clearly reveals a variety of the CT mechanisms in cold ion-atom collisions and orders-of-magnitude variations of their rates. The obvious reason is the strong dependence on tiny electronic properties of a system: a relative potential energy gap between initial and final CT channels, transition dipole moments, and nonadiabatic couplings. It can be inferred that the radiative pathway generally dominates the direct CT process and leads mainly to the formation of a molecular ion. The nonradiative pathway can be competitive if CT occurs to excited states of the products lying close from below to the entrance. The CT processes involving excited ions or atoms [6–8,26,30] may well exhibit a complex interplay of the distinct pathways.

## VI. CONCLUSIONS

High-level scalar-relativistic *ab initio* calculations on the lowest excited electronic states of the  $(\text{YbRb})^+$  ion identified

the direct coupling between the entrance  $A^1\Sigma^+$  and exit  $X^1\Sigma^+$  states as the only pathway for charge transfer in the cold  $\text{Yb}^+(^2S) + \text{Rb}(^2S)$  collisions. Spin-orbit coupling leaves the charge transfer through the entrance  $a1(^3\Sigma^+)$  state inefficient, but modifies the potential energy curve of the  $A$  state to the double-well shape due to avoided crossing with the excited state correlating to the closed  $\text{Yb}^*(^3P^o) + \text{Rb}^+$  charge-transfer asymptote.

Quantum scattering calculations showed that the nonradiative charge transfer induced by radial and angular nonadiabatic coupling matrix elements has a negligible transition probability. Charge transfer proceeds radiatively with the effective rate coefficient  $\sim 3 \times 10^{-14} \text{ cm}^3/\text{s}$ , that is, five orders of magnitude lower than the Langevin capture rate. The calculated radiative cross sections bear all traits of the Langevin regime including the rich structure associated with centrifugal barrier tunneling (orbiting) resonances. The short-range well of the entrance  $A0^+$  state has a weak effect on the charge-transfer efficiency due to decline of the transition moment, but further complicates the resonance structure.

Calculated radiative charge-transfer rate coefficients agree well with the values of  $(4.0 \pm 0.3) \times 10^{-14}$  and  $(2.8 \pm 0.3) \times 10^{-14} \text{ cm}^3/\text{s}$  measured for  $^{174}\text{Yb}^+$  and  $^{172}\text{Yb}^+$  ions, respectively [4]. The observed isotope effect is opposite to that expected from the mass factor for a radiative charge-transfer rate. In our calculations, it is reproduced correctly and originates from the resonance contribution, which increases with the mass of the system. The magnitude of the effect, however, was found to be too small to fully explain the observations.

The calculations estimated the probability to find the product ion  $\text{Rb}^+$  in a trap as  $\sim 30\%$  in agreement with 35% obtained experimentally [4]. The rest of the events correspond to the formation of the bound  $(\text{YbRb})^+$  molecular ion, in sharp contrast to observed loss of the charged particle. Efficient molecular ion photodissociation to highly energetic products by cooling and trapping fields may explain this disagreement.

Present results are in line with the previous studies of similar processes involving alkaline-earth-metal ions and alkali-metal atoms. They suggest that the radiative pathway dominates the ground-state charge transfer having a mean efficiency around  $10^{-5}$  of the Langevin rate and the strong propensity to the molecular ion formation.

## ACKNOWLEDGMENTS

We thank M. Köhl, O. Dulieu, and T. V. Tscherbul for interest and useful discussions, as well as the referee for fruitful comments. This work was partially supported by the Russian Foundation for Basic Research (projects 11-03-00081 and 13-03-00163) and Russian Academy of Sciences (Program of the Fundamental Research by Division of Chemistry and Material Sciences 01 coordinated by Academician O. M. Nefedov).

- [1] S. Willitsch, M. T. Bell, A. D. Gingell, S. R. Procter, and T. P. Softley, *Phys. Rev. Lett.* **100**, 043203 (2008).  
 [2] A. T. Grier, M. Cetina, F. Oručević, and V. Vuletić, *Phys. Rev. Lett.* **102**, 223201 (2009).

- [3] C. Zipkes, S. Palzer, C. Sias, and M. Köhl, *Nature (London)* **464**, 388 (2010).  
 [4] C. Zipkes, S. Palzer, L. Ratschbacher, C. Sias, and M. Köhl, *Phys. Rev. Lett.* **105**, 133201 (2010).

- [5] S. Schmid, A. Härter, and J. H. Denschlag, *Phys. Rev. Lett.* **105**, 133202 (2010).
- [6] W. G. Rellergert, S. T. Sullivan, S. Kotochigova, A. Petrov, K. Chen, S. J. Schowalter, and E. R. Hudson, *Phys. Rev. Lett.* **107**, 243201 (2011).
- [7] F. H. J. Hall, M. Aymar, N. Bouloufa-Maafa, O. Dulieu, and S. Willitsch, *Phys. Rev. Lett.* **107**, 243202 (2011).
- [8] L. Ratschbacher, C. Zipkes, C. Sias, and M. Köhl, *Nat. Phys.* **8**, 649 (2012).
- [9] K. Ravi, S. Lee, A. Sharma, G. Werth, and S. A. Rangwala, *Nat. Commun.* **3**, 1126 (2012).
- [10] F. H. J. Hall, P. Eberle, G. Hegi, M. Raoult, M. Aymar, O. Dulieu, and S. Willitsch, *Mol. Phys.* (2013), doi: 10.1080/00268976.2013.780107.
- [11] Y. Moriwaki, M. Tachikawa, Y. Moeno, and T. Shimizu, *Jpn. J. Appl. Phys.* **31**, L1640 (1992).
- [12] K. Møhlhave and M. Drewsen, *Phys. Rev. A* **62**, 011401(R) (2000).
- [13] O. P. Makarov, R. Côté, H. Michels, and W. W. Smith, *Phys. Rev. A* **67**, 042705 (2003).
- [14] W. W. Smith, O. P. Makarov, and J. Lin, *J. Mod. Opt.* **52**, 2253 (2005).
- [15] R. Côté, *Phys. Rev. Lett.* **85**, 5316 (2000).
- [16] R. Côté and A. Dalgarno, *Phys. Rev. A* **62**, 012709 (2000).
- [17] Z. Idziaszek, T. Calarco, P. S. Julienne, and A. Simoni, *Phys. Rev. A* **79**, 010702 (2009).
- [18] B. Gao, *Phys. Rev. Lett.* **104**, 213201 (2010).
- [19] Z. Idziaszek, A. Simoni, T. Calarco, and P. S. Julienne, *New J. Phys.* **13**, 083005 (2011).
- [20] M. Li and B. Gao, *Phys. Rev. A* **86**, 012707 (2012).
- [21] S. T. Sullivan, W. G. Rellergert, S. Kotochigova, K. Chen, S. J. Schowalter, and E. R. Hudson, *Phys. Chem. Chem. Phys.* **13**, 18863 (2011).
- [22] P. F. Staunum, K. Højbjerg, R. Wester, and M. Drewsen, *Phys. Rev. Lett.* **100**, 243003 (2008).
- [23] S. Willitsch, M. T. Bell, A. D. Gingel, and T. P. Softley, *Phys. Chem. Chem. Phys.* **10**, 7200 (2008).
- [24] F. H. J. Hall and S. Willitsch, *Phys. Rev. Lett.* **109**, 233202 (2012).
- [25] M. Cetina, A. T. Grier, and V. Vuletić, *Phys. Rev. Lett.* **109**, 253201 (2012).
- [26] S. T. Sullivan, W. G. Rellergert, S. Kotochigova, and E. R. Hudson, *Phys. Rev. Lett.* **109**, 223002 (2012).
- [27] P. Zhang, E. Bodo, and A. Dalgarno, *J. Phys. Chem. A* **113**, 15085 (2009).
- [28] P. Zhang, A. Dalgarno, R. Côté, and E. Bodo, *Phys. Chem. Chem. Phys.* **13**, 19026 (2011).
- [29] P. Zhang, A. Dalgarno, and R. Côté, *Phys. Rev. A* **80**, 030703(R) (2009).
- [30] M. Tacconi, F. A. Gianturco, and A. K. Belyaev, *Phys. Chem. Chem. Phys.* **13**, 19156 (2011).
- [31] M. Krych, W. Skomorowski, F. Pawłowski, R. Moszynski, and Z. Idziaszek, *Phys. Rev. A* **83**, 032723 (2011).
- [32] A. Rakshit and B. Deb, *Phys. Rev. A* **83**, 022703 (2011).
- [33] A. K. Belyaev, S. A. Yakovleva, M. Tacconi, and F. A. Gianturco, *Phys. Rev. A* **85**, 042716 (2012).
- [34] Y. Takasu, K. Maki, K. Komori, T. Takano, K. Honda, M. Kumakura, T. Yabuzaki, and Y. Takahashi, *Phys. Rev. Lett.* **91**, 040404 (2003).
- [35] T. Fukuhara, Y. Takasu, M. Kumakura, and Y. Takahashi, *Phys. Rev. Lett.* **98**, 030401 (2007).
- [36] M. H. Anderson, J. R. Ensher, M. R. Matthews, C. E. Wieman, and E. A. Cornell, *Science* **269**, 198 (1995).
- [37] MOLPRO, version 2010.1, a package of *ab initio* programs, H.-J. Werner, P. J. Knowles, R. Lindh, F. R. Manby, M. Schütz, and others (Cardiff, UK, 2010).
- [38] Y. Wang and M. Dolg, *Theor. Chem. Acc.* **100**, 124 (1998).
- [39] M. Dolg, H. Stoll, H. Preuss, and R. M. Pitzer, *J. Phys. Chem.* **97**, 5852 (1993).
- [40] S. M. Cybulski and R. R. Toczyłowski, *J. Chem. Phys.* **111**, 10520 (1999).
- [41] S. F. Boys and F. Bernardi, *Mol. Phys.* **19**, 553 (1970).
- [42] S. R. Langhoff and E. R. Davidson, *Int. J. Quantum. Chem.* **8**, 61 (1974).
- [43] M. Dolg, H. Stoll, and H. Preuss, *J. Chem. Phys.* **90**, 1730 (1989).
- [44] X. Cao and M. Dolg, *J. Mol. Struct.: THEOCHEM* **581**, 139 (2002).
- [45] A. A. Buchachenko, G. Chałasiński, and M. M. Szczeńsiak, *Struct. Chem.* **18**, 769 (2007).
- [46] Yu. Ralchenko, A. E. Kramida, J. Reader, and NIST ASD Team, *NIST Atomic Spectra Database* (ver. 4.0.1) (National Institute of Standards and Technology, 2010), <http://physics.nist.gov/asd>.
- [47] K. Beloy, *Phys. Rev. A* **86**, 022521 (2012).
- [48] A. A. Buchachenko, *Eur. J. Phys. D* **61**, 291 (2011).
- [49] W. F. Holmgren, M. C. Revelle, V. P. A. Lonij, and A. D. Cronin, *Phys. Rev. A* **81**, 053607 (2010).
- [50] J. Deiglmayr, M. Aymar, R. Wester, M. Weidemüller, and O. Dulieu, *J. Chem. Phys.* **129**, 064309 (2008).
- [51] A. K. Belyaev, J. Grosser, J. Hahne, and T. Menzel, *Phys. Rev. A* **60**, 2151 (1999).
- [52] A. Berning, M. Schweizer, H.-J. Werner, P. J. Knowles, and P. Palmieri, *Mol. Phys.* **98**, 1823 (2000).
- [53] N. F. Mott and H. S. W. Massey, *The Theory of Atomic Collisions* (Clarendon Press, Oxford, 1949).
- [54] A. Macias and A. Riera, *Phys. Rep.* **90**, 299 (1982).
- [55] J. Grosser, *Z. Phys. D* **3**, 39 (1986).
- [56] A. K. Belyaev, D. Egorova, J. Grosser, and T. Menzel, *Phys. Rev. A* **64**, 052701 (2001).
- [57] J. Grosser, T. Menzel, and A. K. Belyaev, *Phys. Rev. A* **59**, 1309 (1999).
- [58] A. K. Belyaev, *Phys. Rev. A* **82**, 060701(R) (2010).
- [59] A. K. Belyaev, *Eur. Phys. J. D* **44**, 497 (2007).
- [60] E. Johnson, B. Fricke, T. Jacob, C. Z. Dong, S. Fritzsche, and V. Pershina, *J. Chem. Phys.* **116**, 1862 (2002).
- [61] K. M. Sando, *Mol. Phys.* **21**, 439 (1972).
- [62] P. S. Julienne, *J. Chem. Phys.* **68**, 32 (1978).
- [63] P. S. Julienne and F. H. Mies, *Phys. Rev. A* **34**, 3792 (1986).
- [64] B. Zygelman and A. Dalgarno, *Phys. Rev. A* **38**, 1877 (1988).
- [65] F. A. Gianturco and P. Gori Giorgi, *Astrophys. J.* **479**, 560 (1997).
- [66] J. S. Cohen and J. N. Bardsley, *Phys. Rev. A* **18**, 1004 (1978).
- [67] J. Tellinghuisen and P. S. Julienne, *J. Chem. Phys.* **81**, 5779 (1984).

- [68] M. Gustafsson, S. V. Antipov, J. Franz, and G. Nyman, *J. Chem. Phys.* **137**, 104301 (2012).
- [69] L. Ratschbacher, C. Sias, L. Carcagni, J. M. Silver, C. Zipkes, and M. Köhl, *Phys. Rev. Lett.* **110**, 160402 (2013).
- [70] A. Härter, A. Krüchow, A. Brunner, W. Schnitzler, S. Schmid, and J. H. Denschlag, *Phys. Rev. Lett.* **109**, 123201 (2012).
- [71] F. H. J. Hall, S. Willitsch, M. Aymar, M. Raoult, and O. Dulieu, arXiv:1301.0724.